Physica B 691 (2024) 416271

Contents lists available at ScienceDirect

Physica B: Condensed Matter

journal homepage: www.elsevier.com/locate/physb

# Lattice mismatch effect on electronic and thermodynamic properties of $Si_{0.7}Ge_{0.3}/Si$ self assembled quantum dots with tunable wetting layer

L.M. Pérez [a], M. Kria [b], K. Feddi [c], P. Díaz [d], L. Pedraja-Rejas [a], D. Laroze [e,*], E. Feddi [b,f]

[a] Departamento de Ingeniería Industrial y de Sistemas, Universidad de Tarapacá, Casilla 7D, Arica, Chile
[b] Group of Optoelectronic of Semiconductors and Nanomaterials, ENSAM, Mohammed V University in Rabat, Morocco
[c] Renewable Energy and Advanced Materials Laboratory, International University of Rabat, Morocco
[d] Departamento de Ciencias Físicas, Universidad de La Frontera, Casilla 54-D, Temuco, Chile
[e] Instituto de Alta Investigación, Universidad de Tarapacá, Casilla 7D, Arica, Chile
[f] Institute of Applied Physics, Mohammed VI Polytechnic University, Lot 660, Hay Moulay Rachid Ben Guerir, 43150, Morocco

## ARTICLE INFO

*Keywords:*
SiGe/Si
Prolate
Oblate
Wetting layer
Quantum dot
Thermodynamic properties

## ABSTRACT

During Stransky Kratsanov growth process, quantum dots with non-uniform shapes appear in a random way. Semi-prolate and oblate shapes are among the most likely nanostructures to be self-organized due to their dynamic stability on a substrate. It has been demonstrated that temperature and wetting layer play a very important role in this distribution. In these conditions, physical properties of the deposed semiconductor materials depend on the final structure obtained during the growth process. $Si_{0.7}Ge_{0.3}/Si$ is a semiconductor mainly intended for the manufacture of optoelectronic detectors or in quantum transport. Thus it is important to understand their thermal properties such as heat capacity, entropy and Helmholtz energy. Finite Element Method is used in our calculation to solve numerically the Schrödinger equation for a confined electron in semi-prolate and semi-oblate $Si_{0.7}Ge_{0.3}/Si$ quantum dots. We have taken into account the size of the wetting layer thickness, the strain potential induced by lattice mismatch as well as the temperature. The energy spectrum is then used to determine the thermal characteristics using the statistical Boltzmann–Gibbs distribution. The internal energy of system, entropy, heat capacity, and Helmholtz free energy are determined as a function of the sizes of the quantum dots and wetting layer. The analysis of the behavior of thermodynamic properties presented in this study is considered as complementary and even necessary information to master for a good performance of optoelectronic devices.

## 1. Introduction

Remarkable advances have been witnessed in the past three decades, as investigations focusing on the physics of semiconductor nanostructures in low dimensions has increased greatly [1–5]. These investigations were motivated by the pressing demand for cutting-edge nanofabrication technology. Advanced growth methods including “Chemical Lithography” and “Molecular-Beam Epitaxy” are used to create semiconductor nanostructures [6–8]. Quantum wires, quantum dots, superlattices, single and multi-quantum wells, antidots, pseudodots and other nanostructures are examples of these types of structures [9–15]. Both theoretical and experimental research have paid the aforementioned structures a considerable amount of attention [16–19]. These types of structures present a lot of potential for use in small device applications including lasers and optical modulation technologies, among others [20,21]. Several researchers have looked into the characteristics of these structures using experimental techniques. [22,23]. Additionally, such structures have been applied to a wide range of theoretical investigations, including the prediction of band structure, polaron effects, and transport properties [24–28].

One electrical property of quantum dots (QDs), called energy levels, can be used to hypothetically determine the thermodynamic characteristics of quantum dots [29–31]. Several investigations on the electrical, optical and thermodynamic coefficients of quantum wires with varying cross sections have been conducted over the last ten years [32–40]. The study of thermal properties of semiconductor nanomaterials has attracted the attention of researchers, because these properties can give away like the specific heat capacity, entropy, internal energy, free energy, magnetization, magnetic susceptibility, etc. of the nanomaterial or system [41–44]. Researchers have conducted numerous investigations utilizing both theoretical and experimental methods in this direction [45–48]. A recent development analyzed the effects of the confinement geometry and growth approach on the thermal properties

---

* Corresponding author.
*E-mail address:* dlarozen@academicos.uta.cl (D. Laroze).

https://doi.org/10.1016/j.physb.2024.416271
Received 3 January 2024; Received in revised form 19 June 2024; Accepted 3 July 2024

of these nano-structures [45,49–51]. The effects of the temperature and confinement on the thermodynamic characteristics of the cylindrical core–shell QDs were studied by Kria et al. [52]. The internal energy, entropy, heat capacity, and free Helmholtz energy were evaluated by the authors using the canonical partition function and energy levels. It was discovered that the temperature, dot size, and shell thickness all affect the thermal parameters. Additionally, it was found that the heat capacity behaves abnormally in the thin shell case at low temperatures, but that this impact vanishes for extremely small core radius values. Recently Lakaal et al. [53] used harmonic oscillator as a confinement and electron–electron interaction modeled by Coulomb potential. Following that, under the combined impact of the spin–orbit coupling and electron–phonon interaction, the magnetic and thermodynamic properties of InAs and GaN, which are III-V compounds susceptible to applied a magnetic field, are examined. They showed that the spin interactions lead to a shift of the value for which the magnetic state of the dot changes from paramagnetic to diamagnetic behavior. Besides that, they have shown that the heat capacity exhibits an intriguing anomaly known as the Schottky anomaly, which admits a significant peak at a low temperature.

Khordad et al. [43] investigated the internal energy and entropy of a GaAs cylindrical QDs under the impact of an applied magnetic field. The formalism was useful to obtaining the internal energy and entropy. They are established that the dot radius influences the thermal properties studied. The same authors applied the same approach formalism to investigate thermodynamic properties of quantum wires. It was shown that the thermal properties depend on the temperature and quantum wires size. The authors show that the strong confinement regime leads to discrete nature of thermal prop which turn out to be obvious in nanoscale. It was demonstrated that the entropy and specific heat greatly depend on the Rashba parameter. The effect of temperature, strain and magnetic field on nonextensive entropy of a two-dimensional (2D) quantum dot considering spin–orbit interaction. It was shown that the entropy is raised when the temperature is enhanced with and without strain [54]. It was discovered that the strain does not have strong effect on the entropy at low temperatures. Kuntal et al. [55] investigated the impacts of the magnetic field and finite temperature on non-equilibrium transport in a single molecular transistor using the Anderson–Holstein–Caldeira–Leggett model.

In the aforementioned studies, it has been established that the thermal properties experience noteworthy modifications with confinement. Different physical properties of these nanostructures have been explored widely but there is no study that has focused on the thermodynamic properties of $Si_{0.7}Ge_{0.3}/Si$ quantum dots. To this end, we are particularly interested in closely examining the impacts of wetting layer and dimensions QDs effects on the thermal properties of Semi-prolate and oblate $Si_{0.7}Ge_{0.3}/Si$ quantum dots growth by Stranski–Krastanov process.

This study examines the quantum dot's thermodynamic characteristics. The structure of the present work is as follows: in Section 2, we present a detailed explanation of the fundamental theory, and the thermal properties are calculated by accounting for the statistical canonical ensemble. The quantitative results and a discussion are presented in Section 3. Finally, Section 4 presents with a brief conclusion.

## 2. Background theory

Considering semi-oblate and semi-prolate $Si_{0.7}Ge_{0.3}/Si$ quantum dots, which have been deposited over a Thickness SiGe wetting layer that is caped by a Si matrix with a dimension of $L^3$, where L = 40 nm. Fig. 1 contains the system's schematic. The Schrödinger equation that can be used to explain the following system writes as:

$$\frac{-\hbar^2}{2}\nabla\left[\frac{1}{m_i^*(r)}\nabla\psi(r)\right]+V_w^e(r)\psi(r)+V_s\psi(r)=E\psi(r) \qquad (1)$$

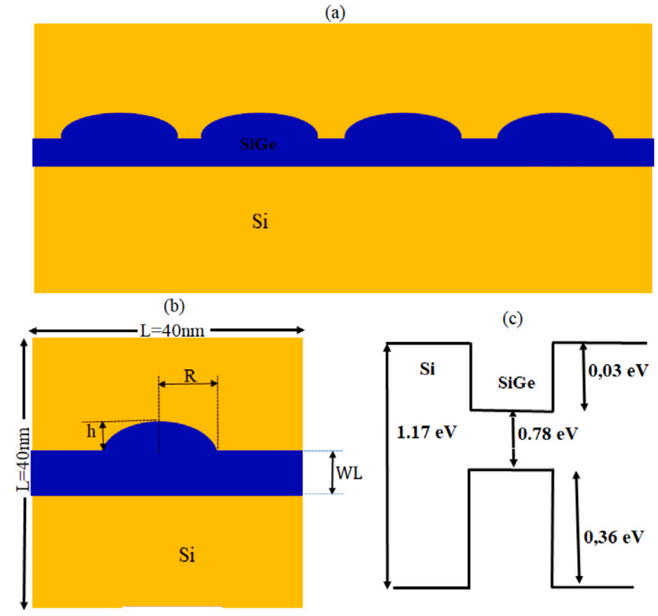

**Fig. 1.** (a) spheroids shape QDs shown in two dimensions. (b) Spheroid QD with $R$, $h$ and WL thickness stand for the radius, height and wetting layer thickness, respectively. (c) The QD energy band diagram.

where the eigenenergies and wave functions respectively, are $\psi(r)$ and $E$. The position-dependent effective mass of the electron is $m_i^*$:

$$m_i^* = \begin{cases} m_{\mathrm{SiGe}}^* & \text{QD+WL} \\ m_{\mathrm{Si}}^* & \text{Matrix} \end{cases} \qquad (2)$$

For both regions, the effective masses of the electrons are defined as function of the two components of the effective masses tensor in the longitudinal and transversal directions noted by $(m_l)$ and $(m_t)$, respectively. In this case, it can be cast in the form [56]:

$$\tilde{m}_e^* = \frac{3m_0}{\frac{1}{m_l}+\frac{2}{m_t}} \qquad (3)$$

where $m_0$ is the electron mass. Let us remark that $Si_{1-x}Ge_x$ behaves like Si material for $x < 0.85$, thus, the effective mass of SiGe is assumed to be the same as that of Si material. Hence, we consider that $m_{\mathrm{SiGe}}^* = 0.26m_0$. Also, let us recall some relevant experimental results reveal that there is a dependence of the effective mass on the temperature. Therefore, the effective mass is well described by the following relation [57]:

$$m_e^* = \frac{\tilde{m}_e^*}{1+\frac{C_i}{E_{g(T,x)}}} \qquad (4)$$

where $C_i = 3.19$ eV. The expression of the temperature-dependent band gap $E_g(T,x)$ is given via Varshni formula and taking into account the x-composition [58]:

$$E_g^{\mathrm{SiGe}}(T) = C_g \times (1-x) \times x + E_g^{\mathrm{Si}}(0) \times (1-x) + E_g^{\mathrm{Ge}}(0) \times x - \frac{\alpha \times T^2}{\beta + T}, \qquad (5)$$

where $E_g^{\mathrm{Ge}}(T=0) = 0.7437$ eV, $E_g^{\mathrm{Si}}(T=0) = 1.166$ eV, $C_g = -0.4$ eV, $\beta = 636$ K and $\alpha = 4.73 \times 10^{-4}$ eV/K.

The confining potential energy $V_w^e(\mathbf{r})$ is given by the difference between the conduction bands of the two materials. It is represented panel (c) of Fig. 1. The expression can be written as:

$$V_w^e(\mathbf{r}) = \begin{cases} 0 & \text{QD+WL} \\ E_C(\mathrm{Si}) - E_C(\mathrm{Si}_{1-x}\mathrm{Ge}_x) & \text{Matrix} \end{cases} \qquad (6)$$

Let us comment that the situation in the conduction band is uncertain. The simultaneous effects of x-concentration and stress effects results produce this uncertainty as to whether the bands align with

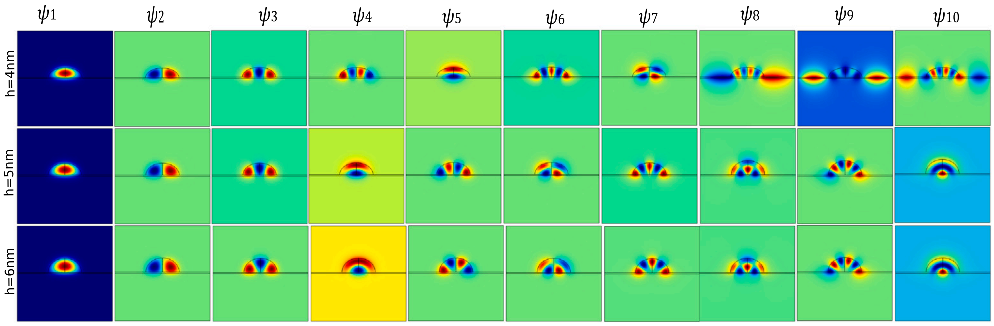

**Fig. 2.** The wavefunction of 10th low lying states of conduction band with a fixed the size of the WL thickness $WL = 0.5$ nm and $L = 40$ nm of oblate QD with height $h = 4, 5$ and 6 nm and radius $R = 7$ nm.

**Table 1**
Parameters of Si, Ge, and $\mathrm{Si_{0.7}Ge_{0.3}}$[56].

| | $m_l^*$ | $m_t^*$ | $\varepsilon$ | $E_g$ (eV) | $a$ (Å) | $C_{11}$ (MPa) | $C_{12}$ (MPa) | $a_v$ (eV) | $b_v$ (eV) |
|---|---|---|---|---|---|---|---|---|---|
| Si | $0.92m_0$ | $0.19m_0$ | 11.9 | 1.17 | 5.431 | 1.675 | 0.650 | 0 | 2.33 |
| Ge | $1.59m_0$ | $0.08m_0$ | 16 | 0.66 | 5.658 | 1.315 | 0.494 | 0 | 2.08 |
| $\mathrm{Si_{0.7}Ge_{0.3}}$ | 0.26 | 0.26 | 13.15 | 0.78 | 5.489 | 1.557 | 0.599 | 0 | 2.25 |

type I or type II. We want to emphasize some studies have been done to clarify this point [59–62]. In particular, an analysis of $\mathrm{Si_{1-x}Ge_x/Si}$ self-assembled islands has been performed using ***k-p*** Hamiltonian with 30 bands for accounting for the strain through the Bir–Pikus formalism [62]. The authors demonstrated that type II or type I band alignment can be found depending on the $x$ and strain effect. The Strain-induced modification of Si/SiGe leads to a significant changes of the band structure. It is known that the band offset between a strained $\mathrm{Si_{1-x}Ge_x/Si}$ film grown on silicon behaves like type I band alignment where the entire band offset occurs in the valence band while the band offset in the conduction band is very small ($E_{C(\mathrm{Si})} - E_{C(\mathrm{Si_{0.7}Ge_{0.3}})} = 30$ meV) [61]. Besides, we notice that in our calculation, the origin of the energy is taken at the bottom of the conduction band of SiGe.

The lattice mismatch $V_s$ produces a strain potential that is specified by [63,64]:

$$V_s = \begin{cases} -D_0 & \text{QD+WL} \\ 0 & \text{Matrix} \end{cases} \tag{7}$$

where $D_0 = a_v^{\mathrm{Si_{1-x}Ge_x}}\varepsilon_\parallel \pm b_v^{\mathrm{Si_{1-x}Ge_x}}\varepsilon_{\parallel\perp}$. (+) symbolizes a light hole and a (−) a heavy hole. $a_v^{\mathrm{Si_{1-x}Ge_x}}$ and $b_v^{\mathrm{Si_{1-x}Ge_x}}$ are the deformation parameters of potential $\mathrm{Si_{1-x}Ge_x}$ and $\varepsilon_\parallel$ and $\varepsilon_{\parallel\perp}$ is given as [63,64]

$$\varepsilon_\parallel = \frac{a_{\mathrm{Si}} - a_{\mathrm{Si_{1-x}Ge_x}}}{a_{\mathrm{Si_{1-x}Ge_x}}}; \qquad \varepsilon_\perp = \varepsilon_\parallel \times \left( -2 \times \frac{C_{12}^{\mathrm{Si_{1-x}Ge_x}}}{C_{11}^{\mathrm{Si_{1-x}Ge_x}}} \right);$$
$$and \ \ \varepsilon_\parallel = \varepsilon_{\parallel\perp} + \varepsilon_\perp \tag{8}$$

where $a_{\mathrm{Si_{1-x}Ge_x}}$ is lattice constant of $\mathrm{Si_{1-x}Ge_x}$ (Si). $C_{11}^{\mathrm{Si_{1-x}Ge_x}}$ and $C_{12}^{\mathrm{Si_{1-x}Ge_x}}$ are the elastic moduli of the compositions $\mathrm{Si_{1-x}Ge_x}$. Table 1 contains the values for the elastic moduli, lattice constant and deformation potential parameters.

The Schrödinger equation's analytical solution is highly difficult or even impossible to achieve given the shapes of these type of nanostructures. We can avoid this problem by using the finite element approach to solve the Schrödinger equation while adhering to established the boundary conditions.

Once the energy spectrum has been determined by solving Schrödinger equation, we proceed to the determination the partition function $Z_c$ given in the Boltzmann–Gibbs distribution. The sum of all energy states can be used to compute it [65]:

$$Z_c = \sum_\nu e^{-\beta E_\nu} \tag{9}$$

where $\beta = 1/(k_B \times T)$ is the inverse temperature, $k_B$ is the Boltzmann constant and $E_\nu$ present the all states eigenvalues of quantum dot such as $H|\nu\rangle = E_\nu|\nu\rangle$.

The mean energy of electron at constant volume is given by:

$$\langle E \rangle = -\frac{\partial \ln Z_c}{\partial \beta}. \tag{10}$$

$Z_c$ can be used to determine the system's specific heat, which indicates how much energy can be saved in the system per degree of temperature increase, together with all other thermodynamic properties of the system. The relation results in:

$$C_v = -k_B \beta^2 \left( \frac{\partial \langle E \rangle}{\partial \beta} \right). \tag{11}$$

The entropy S, which gauges how random the system is, is the second significant thermodynamic feature.

$$S = \frac{\langle E \rangle - F_H}{T}, \tag{12}$$

where $F_H = \frac{-\ln Z_c}{\beta}$ is the Helmholtz free energy, which serves as the stability requirement and is crucial for understanding the structure.

## 3. Results and discussion

The Finite Element Method is used to numerically solve Eq. (1) using the COMSOL Multiphysics software [66]. The Schrödinger equation is developed in the part of the Partial Differential Equation (PDE). According to Fig. 1a, we use 8 borders, represented by the symbol $B_i$ with $i = 1, \dots, 8$, to define the boundaries between the various parts of the structure. Using the following guidelines, the eigenvalue solver was employed: The boundary conditions used in our studies is the Dirichlet condition ($\psi = 0$) was applied at the six limit lateral borders ($B_2, B_3, B_4, B_6, B_7, B_8$), and the Neumann condition ($\hat{n} \cdot \nabla\psi = 0$) at two lateral limit($B_1, B_5$). Notably, we employed a highly refined meshing with ∼14400 degrees of nodes. According to experimental reports, the size of the WL thickness was fixed at 0.5 nm [67]. The explanation of the findings as shown in Figs. 2–8 will take up much of this section.

Figs. 2 and 3 represent the xy projection of the wave functions of the 10th low states. The color scale is defined with red at a positive maximum value, and the negative maximum with blue. From Fig. 2, it is observed that the $\psi_1$ and $\psi_2$ are symmetrical for three height semi-oblate h = 4, 5 et 6 nm. $\psi_1$ have s-like symmetry and $\psi_2$ have p-like symmetry for three sizes h = 4, 5 and 6 nm, $\psi_4$ have d-like symmetry (h = 4 nm), $\psi_6$ (h=4 nm) and $\psi_7$ (h=5 and 6 nm) have f-like symmetry.

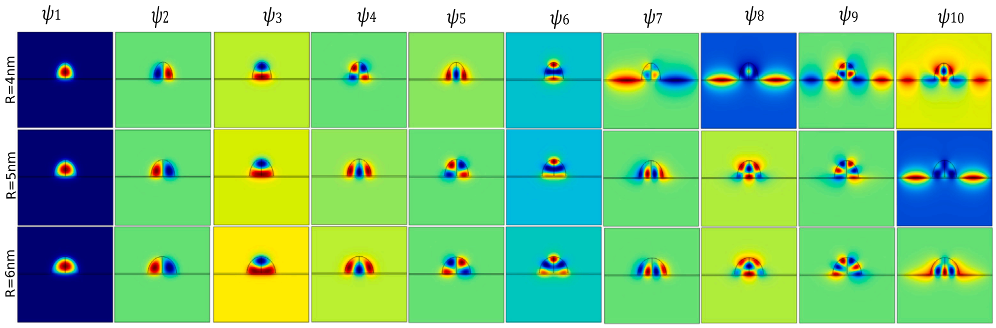

**Fig. 3.** The wavefunction of 10th low lying states of conduction band with a fixed size wetting layer thickness $WL = 0.5$ nm and size of matrix $L = 40$ nm of prolate QD with radius $R = 4, 5$ and 6 nm and height $h = 7$ nm.

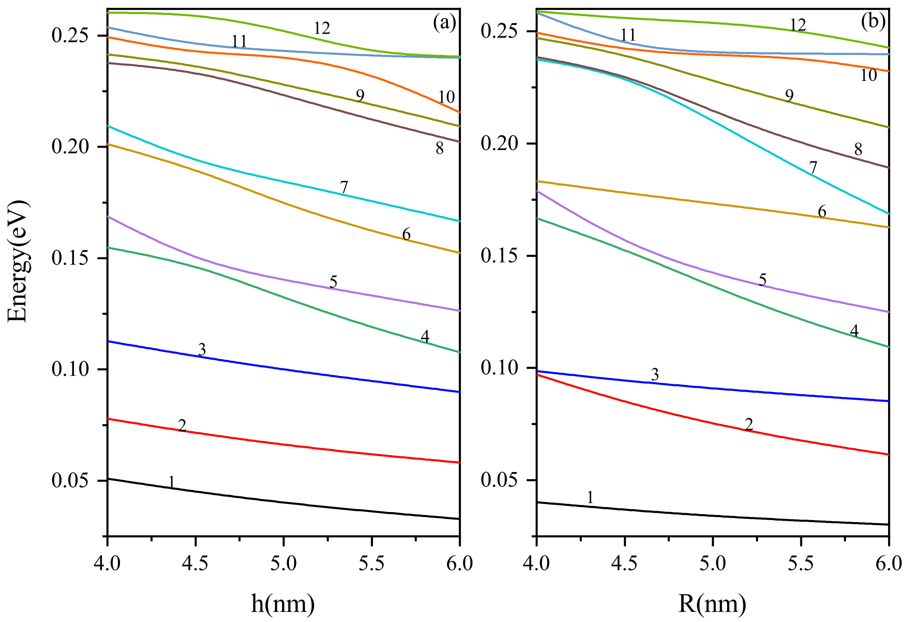

**Fig. 4.** Ground and excited state eigenenergies versus (a) oblate height $h$ for a fixed radius $R = 7$ nm; (b) versus prolate radius $R$ for a fixed height $h = 7$ nm.

We can see in panel of the wave functions $\psi_8$, $\psi_9$ and $\psi_{10}$ (4 nm) that the electron can be assigned both in the central region of the dot and in the wetting layer. It should be noted here that $\psi_7$, $\psi_8$ and $\psi_9$ double the number of antinods $\psi_2$ and $\psi_3$ for the three sizes, which is in agreement with their higher energy. Furthermore, the inset in Fig. 3 shows also the evolution of the ten lowest electron states. As we can see, the wave functions $\psi_1$ and $\psi_2$ are symmetrical for three height semi-prolate h = 4, 5 et 6 nm. For three sizes of radius semi-prolate R = 4, 5 et 6 nm, in panel of the wave functions $\psi_7$, $\psi_8$, $\psi_9$ and $\psi_{10}$ the electron can be assigned in WL.

It is important to not that our numerical calculations of the partition function $Z_c$ show that the saturation of the summation in the expression of $Z_c$ depends on the energy levels and consequently it is related to the radius R and height h. Strictly speaking the convergence of the summation of Zc is obtained since the 10th levels (by considering 9 digits) this is why we restricted our developments to the lowest 12th terms.

In Fig. 4, the energies of the twelve lowest confined electron states in a $\mathrm{Si_{0.7}Ge_{0.3}/Si}$ are depicted as functions of the inner semi-oblate height and -Prolate radius. It is observed that all energy levels decrease as long as $h$ and $R$ augments. It is observed that all energy levels decrease as long as h and R augments. This is due to the progressive increase in the volume of the dot $\mathrm{Si_{0.7}Ge_{0.3}/Si}$ where the confinement of electron decreases. We notice that the levels 7 and 8 are twice degenerate for sizes semi-prolate $R = 4$ and 4.5 nm.

In Fig. 5a (solid curves), we present the variation of the mean energies versus temperature for oblate system corresponding to three values of height $h = 4, 5$ and 6 nm and for a fixed radius size $R = 7$ nm. In Fig. 5a (dashed curves), we present the variation of the mean energies versus temperature for prolate system corresponding to three values of prolate radius $R = 4, 5$ and 6 nm and for a fixed radius size $h = 7$ nm. Fig. 5b shows the variation of the mean energies as a function of the temperature $T$ for three values of the wetting layer $WL = 0.5, 1$ and 1.5 nm and for a fixed values of $h = 5$, and $R = 7$ nm for oblate system and for a fixed values of the hight $h = 7$, and $R = 5$ nm for prolate system. The mean energies is observed to increase as the temperature increases, but it (mean energy) decreases as the oblate height h and prolate radius R of the QD increases i.e. the confinement becomes very strong and its energy increases strongly. Moreover, the mean energy of semi-oblate is more pronounced than semi-prolate because the volume of the semi oblate is large so the electron becomes less confined in the prolate and its energy is reduced. Fig. 5b shows that the mean energy rises with rising temperature and again declines as prolate radius R rises. We observed that the mean energies in both cases remained constant till the temperature rise to $T \sim 50$ K and T = 75 K as shown in Fig. 5a. It can be inferred that the variation of the oblate and prolate size makes the mean energy to be constant in the low temperature regime. The mean energies increases in the relatively high temperature region. In addition, it is seen that an increase in wetting layer thickness decreases the mean energies, as shown in Fig. 5b. The response of the

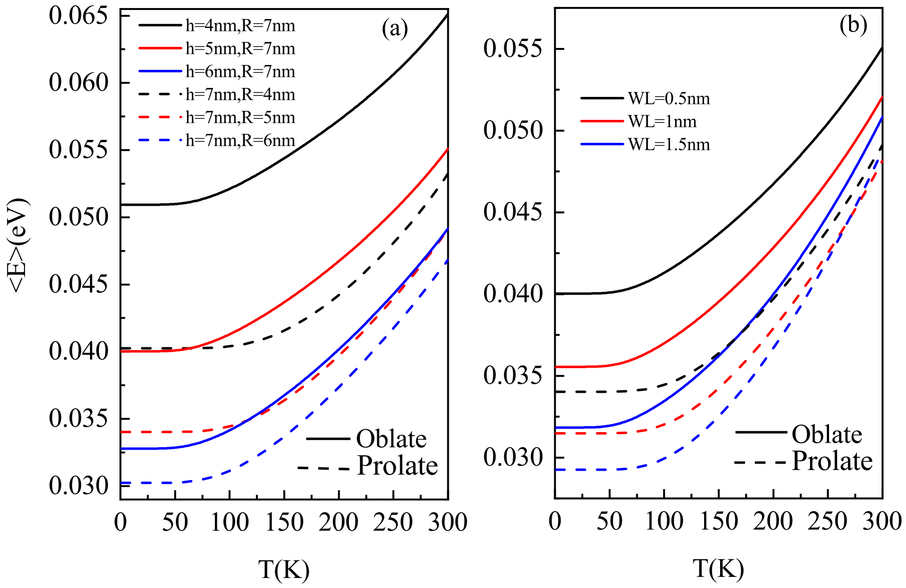

**Fig. 5.** (a) Mean energies versus temperature for three values of the height (oblate) $h = 4, 5$ and $6\,\text{nm}$ with $R = 7\,\text{nm}$ (solid line); and three values of the radius (prolate) $R = 4, 5$ and 6 nm with $h = 7\,\text{nm}$ (dashed line). (b) Mean energies versus temperature for three values of Wetting layer thickness $WL = 0.5, 1$ and $1.5\,\text{nm}$ for oblate ($h = 5\,\text{nm}$, $R = 7\,\text{nm}$) and prolate ($h = 7\,\text{nm}$, $R = 5\,\text{nm}$).

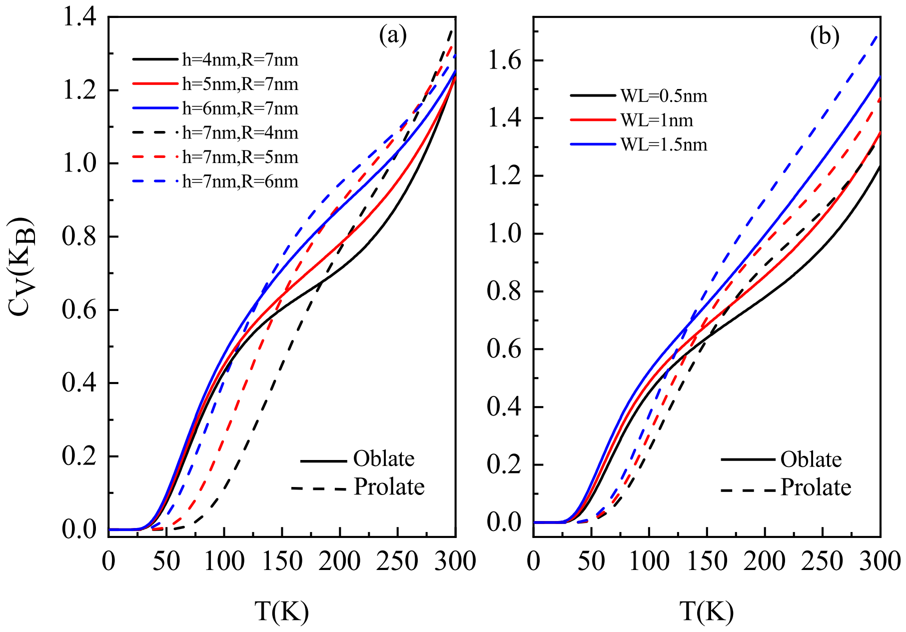

**Fig. 6.** Specific heat versus temperature for three values of the height (oblate) $h = 4, 5$ and $6\,\text{nm}$ with a fixed radius $R = 7\,\text{nm}$ (solid line); and three values of the radius (prolate) $R = 4, 5$ and 6 nm with a fixed height $h = 7\,\text{nm}$ (dashed line). (b) Specific heat versus temperature for three dimensions Wetting layer thickness $WL = 0.5, 1$ and 1.5 nm for oblate ($h = 5\,\text{nm}$, $R = 7\,\text{nm}$) and prolate ($h = 7\,\text{nm}$, $R = 5\,\text{nm}$).

mean energies to temperature variation is seen to be increasing. One could say that the oblate height ($h = 5\,\text{nm}$, $R = 7\,\text{nm}$), for prolate radius ($R = 5\,\text{nm}$, $h = 7\,\text{nm}$) and wetting layer thickness influences the QD in the same way.

Fig. 6a displays the specific heat as a function of the temperature for QD for various oblate height $h = 4, 5$ and $6\,\text{nm}$ for a fixed radius size $R = 7\,\text{nm}$ and prolate radius $R = 4, 5$ and 6 nm for a fixed height size $h = 7\,\text{nm}$. Up to $T \sim 25$ K, the specific heat is constant but beyond this region, $T > 25$ K, the specific heat rises with rising temperature for semi-oblate. For semi-prolate the Cv is constant at low temperature ($T \sim 25$ K). Interestingly, an increase in the oblate height and prolate radius of the QDs also increases the specific heat. In addition the Cv of oblate is more than prolate until the critical values of temperature. This behavior in Cv is reversed after the critical temperature which is $T = 125, 150$ and $175\,\text{K}$. A thorough examination of the behavior reveals that it deviates from the Duolong–Petit rule because the specific heat does not saturate at high temperatures, despite the fact that one may claim that on average, the specific increases with increasing temperature. This anomaly could be attributed to Schokky anomaly [68–70], which can also attributed to the lattice deformation due to the strain effect existing between different materials constituting the structures. This behavior observed above is seen Fig. 6b, where the wetting layer thickness was varied from $WL = 0.5$ until 1.5 nm. It is

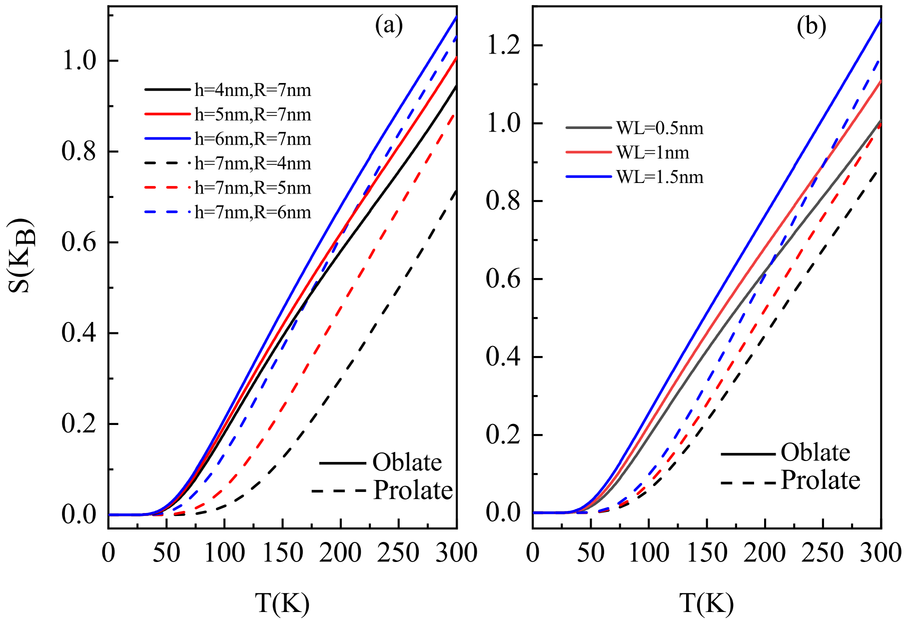

**Fig. 7.** Entropy versus temperature for three values of height (oblate) $h = 4, 5$ and $5\,\mathrm{nm}$ with a fixed radius $R = 7\,\mathrm{nm}$ (solid line); and three values of radius (prolate) $R = 4, 5$ and 6 nm with a fixed height $h = 7\,\mathrm{nm}$ (dashed line). (b) Entropy versus temperature for three dimensions of Wetting layer thickness $WL = 0.5, 1$ and 1.5 nm for oblate ($h = 5\,\mathrm{nm}$, $R = 7\,\mathrm{nm}$) and prolate ($h = 7\,\mathrm{nm}$, $R = 5\,\mathrm{nm}$).

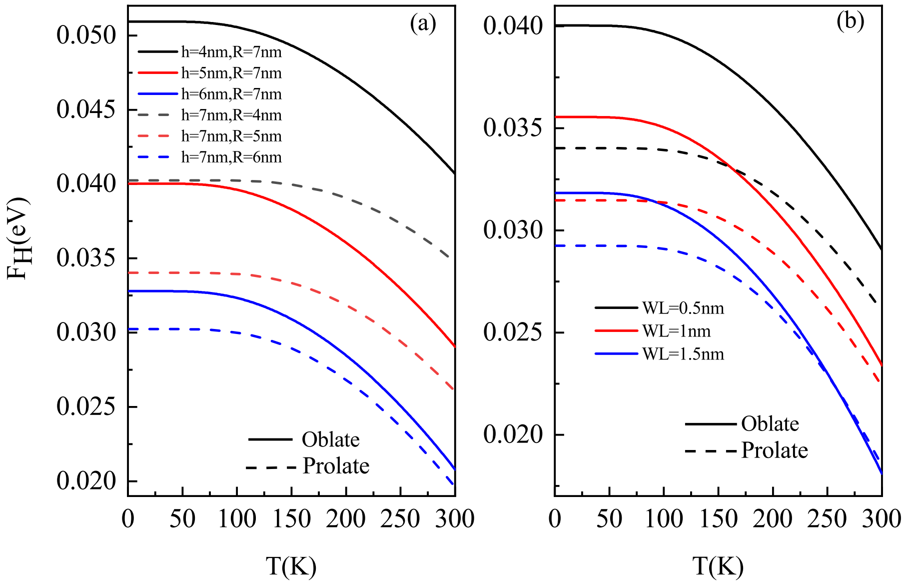

**Fig. 8.** Helmholtz free energy as a function of the temperature for three values of the height $h = 4, 5$ and $5\,\mathrm{nm}$ with $R = 7\,\mathrm{nm}$ (solid line); and three values of the radius $R = 4, 5$ and 6 nm with $h = 7\,\mathrm{nm}$ (dashed line). (b) Helmholtz free energy versus temperature for three sizes of Wetting layer thickness $WL = 0.5, 1$ and 1.5 nm for oblate ($h = 5$ nm, $R = 7\,\mathrm{nm}$) and prolate ($h = 7\,\mathrm{nm}$, $R = 5\,\mathrm{nm}$).

also seen that the specific heat increases as the wetting layer rises and also rises with rising temperature.

Fig. 7a shows the entropy versus temperature with various values of the oblate height $h = 4, 5$ and $5\,\mathrm{nm}$ for a fixed radius size $R = 7\,\mathrm{nm}$. For prolate radius $R = 4, 5$ and 6 nm with a fixed height size $h = 7\,\mathrm{nm}$. The entropy was constant up to $T \sim 25$ K for oblate and $T \sim 50$ K for prolate. Beyond this point, it is observed that the entropy increases with rising temperature. These findings can be explained utilizing various laws of thermodynamics. In the first instance, The Nernst–Simon interpretation of the third law of the thermodynamics, which deals with thermodynamic processes at a given low temperature, states that no thermal process, no matter how ideal the conditions, can reduce a system's entropy to zero in a finite number of operations [71].

Fig. 7a illustrates how the entropy of the system approaches a constant value as its temperature approaches absolute zero. Due to the increasing thermal energy of the electrons in the quantum dot, which results in a similar disorderliness in the form of random motion, the continuous rise in entropy as the temperature increases demonstrates its conformity with the second law of thermodynamics [65]; other authors for this behavior of the entropy include the generalized second law of thermodynamics [72]. Furthermore, to investigate the effects of the wetting layer thickness on the entropy, also it is plotted against temperature with various values of the wetting layer thickness (Fig. 7b). Again the entropy first displays a constant trend and then increases with increasing temperature. Interestingly, the wetting layer thickness increases the entropy as its increases. This is true because as the thickness increases, the electrons will need more thermal energy to move randomly in the zero-dimensional structure.

Fig. 8a shows the plot of the Helmholtz free energy versus temperature with various oblate heights $h = 4, 5$ and $5\,\mathrm{nm}$ for a fixed radius size $R = 7\,\mathrm{nm}$ and prolate radius $R = 4, 5$ and $6\,\mathrm{nm}$ for a fixed height size $h = 7\,\mathrm{nm}$. It is important to point out here that the stability quantum dots is described by the Helmholtz free energy. The free energy decreases with rising temperature although a constant trend was observed in the relatively low temperature regime. More specifically, when the oblate height and prolate radius rises, the free energy diminishes. The stability condition states that if a system's Helmholtz energy is low, it is stable. So the structure prolate is more stable than oblate; This result can be attributed to the lattice deformation effect. The free energy satisfies this requirement, as can be seen by carefully observing the numerical values on the scale of our plots. Fig. 8b, which analyzes various values of the prolate radius and wetting layer thickness, shows the same behavior of the free energy as described above. Moreover, the Helmholtz energy of oblate is more than prolate; hence the prolate structure is more stable than the prolate.

## 4. Conclusion

In this study we examined how the size, Wetting layer, and possible lattice mismatch affect the thermodynamic characteristics of semi-oblate and semi-prolate quantum structures. We investigated the energy states numerically by Finite Element Method to calculate the partition function. Then, we calculated the average energy, entropy, heat capacity, and Helmholtz free energy. Our results further demonstrate that the thermodynamic coefficients depend strongly on parameters of quantum structures and lattice mismatch effect. As an important remark, the wetting layer thickness increases the entropy as its increases because the thickness increases. The electrons will need more thermal energy to move randomly in the zero-dimensional structure. Concerning the stability of structures, the semi-prolate and semi-oblate QDs have more stable structures in large sizes because the Helmholtz free energy $F_H$ is larger for smaller sizes. Semi-prolate has a more stable structure because $F_H$ is bigger than that of semi-oblate.

## CRediT authorship contribution statement

**L.M. Pérez:** Writing – review & editing, Investigation, Conceptualization, Funding acquisition. **M. Kria:** Writing – original draft, Visualization, Software, Methodology, Investigation, Formal analysis. **K. Feddi:** Software, Methodology, Investigation, Formal analysis. **P. Díaz:** Visualization, Validation, Investigation. **L. Pedraja-Rejas:** Visualization, Validation, Investigation. **D. Laroze:** Writing – review & editing, Supervision, Project administration, Methodology. **E. Feddi:** Writing – original draft, Validation, Supervision, Project administration, Methodology, Investigation, Conceptualization.

## Declaration of competing interest

The authors declare that there is not a conflict of interest.

## Data availability

No data was used for the research described in the article.

## Acknowledgments

LMP acknowledges financial support from ANID through Convocatoria Nacional Subvención a Instalación en la Academia Convocatoria Año 2021, Grant SA77210040. LMP and DL acknowledge partial financial support from ANID through FONDECYT 1240985. LMP, PD, and DL acknowledge partial financial support from ANID through FONDECYT 1231020.

## References

[1] M.T. Sandoval, G.C. La Rocca, E.D.A. Silva, Phys. E Low Dimens. Syst. Nanostruct. 138 (2022) 115061.
[2] K. Ullah, Y. Meng, Y. Shi, F. Wang, Adv. Opt. Mater. (2022) 2101860.
[3] M.A. Roudbari, T.D. Jorshari, C. Lü, R. Ansari, A.Z. Kouzani, M. Amabili, Thin-Walled Struct. 170 (2022) 108562.
[4] M. Yang, H. Jin, Z. Sun, R. Gui, J. Mater. Chem. 10 (2022) 5111.
[5] Y. Qi, S. Yang, J. Wang, L. Li, Z. Bai, Y. Wang, Z. Lv, Mater. Today Phys. 23 (2022) 100622.
[6] E. Rotenberg, B.K. Freelon, H. Koh, A. Bostwick, K. Rossnagel, A. Schmid, S.D. Kevan, New J. Phys. 7 (2005) 114.
[7] A.M. Gil, A. Rota, T. Maroutian, B. Bartenlian, P. Beauvillain, E. Moyen, M. Hanbucken, Superlattices Microstruct. 36 (2004) 235.
[8] S. Axelsson, E.E.B. Campbell, L.M. Jonsson, J. Kinaret, S.W. Lee, Y.W. Park, M. Sveningsson, New J. Phys. 7 (2005) 245.
[9] A. Cetin, Phys. Lett. A 372 (2008) 3852.
[10] N. Aquino, E. Castano, E. Ley-Koo, Chin. J. Physiol. 41 (2003) 276.
[11] E.N. Bogachek, U. Landman, Phys. Rev. B 52 (1995) 14067.
[12] A.D. Chepelianskii, D.L. Shepelyansky, Phys. Rev. B 63 (2001) 165310.
[13] A. Matulis, T. Pyragiene, Phys. Rev. B 67 (2003) 045318.
[14] S. Ikhdair, R. Sever, J. Mol. Struct. 806 (2007) 155.
[15] J. Reijniers, F.M. Peeters, A. Matilus, Phys. Rev. B 59 (1998) 2817.
[16] F. Niley, K. Nakamura, Phys. B 184 (1993) 398.
[17] D. Weiss, K. Richiter, A. Manschig, R. Bergman, H. Schweizer, K. von Klitzing, Phys. Rev. Lett. 70 (1993) 4118.
[18] B. Chayanika, J. Appl. Phys. 6 (1998) 3089.
[19] K. Lisa, S. Bednareka, B. Szafrana, J. Adamowski, Phys. E Low Dimens. Syst. Nanostruct. 17 (2003) 494.
[20] S. Ijima, Nature 54 (1991) 56.
[21] H.W. Kroto, S.R. O'Brein, R.F. Curl, R.E. Smalley, Nature 318 (1985) 162.
[22] M. Tanaka, H. Yamada, T. Maruyama, K. Akimoto, Phys. Rev. B 67 (2003) 045305.
[23] E. Räsänen, H. Saarikoski, V.N. Stavrou, A. Harju, M.J. Puska, R.M. Nieminen, Phys. Rev. B 67 (2003) 235307.
[24] R. Khordad, Phys. E 41 (2009) 543.
[25] R. Khordad, A. Gharaati, M. Haghparast, Curr. Appl. Phys. 10 (2010) 199.
[26] B. Vaseghi, R. Khordad, M.M. Golshan, Phys. Status Solidi b 243 (2006) 2772.
[27] E. Sadeghi, R. Khordad, Braz. J. Phys. 36 (2006) 1213.
[28] E. Sadeghi, R. Khordad, Phys. Status Solidi b 242 (2005) 1628.
[29] N.K. Datta, M. Ghosh, Chem. Phys. 372 (2010) 82.
[30] A. Bera, S. Saha, J. Ganguly, M. Ghosh, Chem. Phys. 474 (2016) 36.
[31] S. Saha, J. Ganguly, A. Bera, M. Ghosh, Chem. Phys. 480 (2016) 17.
[32] R. Khordad, Int. J. Thermophys. 34 (2013) 1148.
[33] R. Khordad, Contin. Mech. Thermodyn. 28 (2016) 947.
[34] R. Khordad, H.R. Rastegar Sedehi, Superlattices Microstruct. 101 (2017) 559.
[35] R. Khordad, H.R. Rastegar Sedehi, Indian J. Phys. 91 (2017) 825.
[36] M. Choubani, H. Maaref, F. Saidi, J. Phys. Chem. Solids 138 (2020) 109226.
[37] M. Choubani, H. Maaref, F. Saidi, Eur. Phys. J. Plus 137 (2) (2022) 265.
[38] R. Khordad, H.R. Rastegar Sedehi, Indian J. Phys. 92 (2018) 979.
[39] R. Khordad, H.R. Rastegar Sedehi, J. Low Temp. Phys. 190 (2018) 200.
[40] R. Khordad, H.R. Rastegar Sedehi, Solid State Commun. 269 (2018) 118.
[41] C.O. Edet, A.N. Ikot, M.C. Onyeaju, U.S. Okorie, G.J. Rampho, M.L. Lekala, S. Kaya, Phys. E Low Dimens. Syst. Nanostruct. 131 (2021) 114710.
[42] C.O. Edet, A.N.A.N. Ikot, Mol. Phys. 119 (2021) 1957170.
[43] R. Khordad, C.O. Edet, A.N. Ikot, Internat. J. Modern Phys. C (2022) 2250106.
[44] C.O. Edet, A.N. Ikot, J. Low Temp. Phys. 203 (2021) 84–111.
[45] T. Juntunen, T. Koskinen, V. Khayrudinov, T. Haggren, H. Jiang, H. Lipsanen, I. Tittonen, Nanoscale 11 (2019) 20507.
[46] K.A. Ritter, J.W. Lyding, Nature Mater. 8 (2009) 235.
[47] A.M. Mirsaeidi, F. Yousefi, J. Therm. Anal. Calorim. 143 (2021) 351.
[48] A. Rashidi, B. Ghobadian, G. Najafi, M.H. Khoshtaghaza, N.A.C. Sidik, A. Yadegari, H.W. Xian, Int. Commun. Heat Mass Transfer 90 (2018) 85.
[49] A.I. Boukai, Y. Bunimovich, J. Tahir-Kheli, J.-K. Yu, W.A. Goddard Iii, J.R. Heath, Nature 451 (2008) 168.
[50] L. Yin, E. Kyung Lee, J. Woon Lee, D. Whang, B. Lyong Choi, C. Yu, Appl. Phys. Lett. 101 (2012) 043114.
[51] J. Chen, G. Zhang, B. Li, Nano Lett. 12 (2012) 2826.
[52] M. Kria, K. Feddi, N. Aghoutane, M. El-Yadri, L.M. Pérez, D. Laroze, F. Dujardin, E. Feddi, Phys. A 560 (2020) 125104.
[53] K. Lakaal, M. Kria, J. El Hamdaoui, Varsha, V. Prasad, V.V. Nautiyal, M. El-Yadri, L.M. Pérez, D. Laroze, E. Feddi, J. Magn. Magn. Mater. 551 (2022) 169042.
[54] R. Khordad, R. Bornaei, H.A. Mardani-Fard, Indian J. Phys. (2014).
[55] K. Bhattacharyya, M. Kalla, A. Chatterjee, Mater. Today Proc. 55 (1) (2022).
[56] M.E. Levinshtein, L.R. Sergey, S.S. Michael, Properties of Advanced Semiconductor Materials: GaN, AIN, InN, BN, SiC, SiGe, John Wiley & Sons, 2001.
[57] Y. Yu Peter, M. Cardona, Fundamentals of Semiconductors, Springer, Berlin, 1988.
[58] G.A. Armstrong, C.K. Maiti, Technology Computer Aided Design for Si, SiGe and GaAs Integrated Circuits, Vol. 21, IET, 2007.

[59] K.Y. Wang, P.W. Huang, H.H. Cheng, G. Sun, R.A. Soref, R.J. Nicholas, Y.W. Suen, Appl. Phys. Lett. 91 (7) (2007).
[60] R. People, IEEE J. Quantum Electron. 22 (9) (1986) 1696–1710.
[61] C.K. Maiti, K.L. Bera, S. Chattopadhyay, Semicond. Sci. Technol. 13 (11) (1998) 1225.
[62] M. El Kurdi, S. Sauvage, G. Fishman, P. Boucaud, Phys. Rev. B 73 (19) (2006) 195327.
[63] J.L. Liu, J. Zhu, J. Appl. Phys. 101 (2007) 093709.
[64] K. Lakaal, M. Kria, J. El Hamdaoui, V. Prasad, E. Feddi, D. Laroze, M.E. Ramos, Eur. Phys. J. Plus 137 (2022) 1.
[65] F.S. Nammas, Phys. A 508 (2018) 187.
[66] COMSOL Multiphysics software version 5.2 (www.comsol.com).
[67] Y. Yu, X.-J. Shang, M.-F. Li, G.-W. Zha, J.-X. Xu, L.-J. Wang, G.-W. Wang, H.-Q. Ni, X. Dou, B. Sun, Appl. Phys. Lett. 102 (2013) 201103.
[68] J.D. Castano-Yepes, C.F. Ramirez-Gutierrez, H. Correa-Gallego, E.A. Gómez, Physica E 103 (2018) 464.
[69] J.D. Castano-Yepes, D.A. Amor-Quiroz, C.F. Ramirez-Gutierrez, E.A. Gómez, Physica E 109 (2019) 59–66.
[70] R.B. Adhikari, P. Shen, D.L. Kunwar, I. Jeon, M.B. Maple, M. Dzero, C.C.C.C. Almasan, Phys. Rev. B 100 (2019) 174509.
[71] W. Jost, Physical Chemistry an Advanced Treatise, Elsevier, 1971, p. 684.
[72] F.Q. Tu, Y.X. Chen, Q.H.Q.H. Huang, Entropy 21 (2019) 167.